ADVANCED MATERIALS INTERFACES
www.advmatinterfaces.de

Nanoscale Chemical and Valence Evolution at the Metal/Oxide Interface: A Case Study of Ti/$SrTiO_3$

*Yangyang Li, Qingxiao Wang, Ming An, Kun Li, Nimer Wehbe, Qiang Zhang, Shuai Dong, and Tom Wu**

Metal/oxide interfaces are ubiquitous in a wide range of applications such as electronics, photovoltaics, memories, catalysis, and sensors. However, there have been few investigations dedicated to the nanoscale structural and chemical characteristics of these buried interfaces. In this work, the metal/oxide interface between Ti and $SrTiO_3$ (STO) is examined as a prototypical system using high-resolution scanning transmission electron microscopy and electron energy loss spectroscopy. An atomic-thin Ti_2O_3-like layer at the Ti/STO interface prepared at room temperature is discovered, and first-principles calculations predict a metallic band structure of this 2D electron system. As a universal feature of such interfaces prepared at different temperatures, near the interface nanoscale oxygen-deficient domains and continuous modulation of Ti oxidation states are found. Overall, these results directly reveal complex chemical and valence evolutions at the metal/oxide interfaces, providing microscopic insights on such heterostructures.

1. Introduction

Interactions between metals and oxides at their interfaces are key factors determining the performance of metal/oxide heterojunctions, which are ubiquitous in modern technologies including electronics, photonics, catalysis, energy conversion, sensors, and so on. It is well recognized that metal/semiconductor interfaces must be properly prepared and controlled in order to achieve the optimal performance in functional devices. For example, ohmic contacts play a key role in the fabrication of high-performance optoelectronics such as light emitting diodes and laser diodes.[1–3] Such transparent contacts allow high charge injection and improve thermal stability, which is critical for reliable device operation. Electrodes with different metals and their combinations have been extensively explored,[4–8] which motivated researchers to examine the microscopic structures of the interfaces between semiconductors and metals.

Functional oxides have a broad range of technological applications due to their unique properties such as ferroelectricity, piezoelectricity, high-T_C superconductivity, colossal magnetoresistance, and so on. Particularly, forming reliable, low-resistance ohmic contacts are of critical importance to the advancement of oxide electronics. Majority of metals form Schottky barriers when deposited on oxide surfaces.[9–11] Among functional oxides, Ti-based oxides including titanium dioxide (TiO_2) and strontium titanium oxide ($SrTiO_3$/STO) are widely investigated. STO is well known not only as popular substrate for film growth, but also for many interesting properties, such as superconductivity,[12] blue-light emission,[13–15] insulator–metal transition,[16] and photocatalytic properties.[17] Recently, STO has also been explored for resistive switching memory[18] and optoelectronic applications.[19–21] Ti is one of the earth-abundant elements, and it is frequently used to form contacts with oxides. Although the importance of metal/oxide interfaces has been well recognized,[22–24] there have been few works devoted to understanding the microscopic phenomena at such buried interfaces.

In this work, we investigated the Ti/STO interfaces as a prototypical system using a series of complimentary imaging tools including high-resolution high-angle annular dark field (HAADF) and low-angle annular dark field (LAADF) scanning transmission electron microscopy (STEM), electron energy loss spectrum (EELS), and secondary ion mass spectrometry (SIMS). We observed substantial oxygen interdiffusion at the metal/oxide interface, which is accompanied by the gradual evolution of the Ti valence from 4^+, 3^+ to 0. Importantly, we discovered atomic-thin layer of cubic perovskite Ti_2O_3 (Ti^{3+}) and anatase TiO_2 (Ti^{4+}) at the interfaces prepared at room temperature and 200 °C, respectively. Overall, our in-depth atomic-scale characterizations of the Ti/STO interfaces provide valuable structural and chemical information for such heterostructures, which could be generalized to the investigation of other interface systems.

Y. Y. Li, Q. Zhang, Prof. T. Wu
Materials Science and Engineering
King Abdullah University of Science and Technology
Thuwal 23955-6900, Kingdom of Saudi Arabia
E-mail: tao.wu@kaust.edu.sa
Q. X. Wang
Department of Materials Science and Engineering
University of Texas at Dallas
800 W. Campbell Rd., RL10 Richardson, TX 75080, USA
Dr. M. An, Prof. S. Dong
Department of Physics
Southeast University
Nanjing 211189, China
Dr. K. Li, Dr. N. Wehbe
Imaging & Characterization Core Lab
King Abdullah University of Science and Technology
Thuwal 23955-6900, Kingdom of Saudi Arabia

DOI: 10.1002/admi.201600201

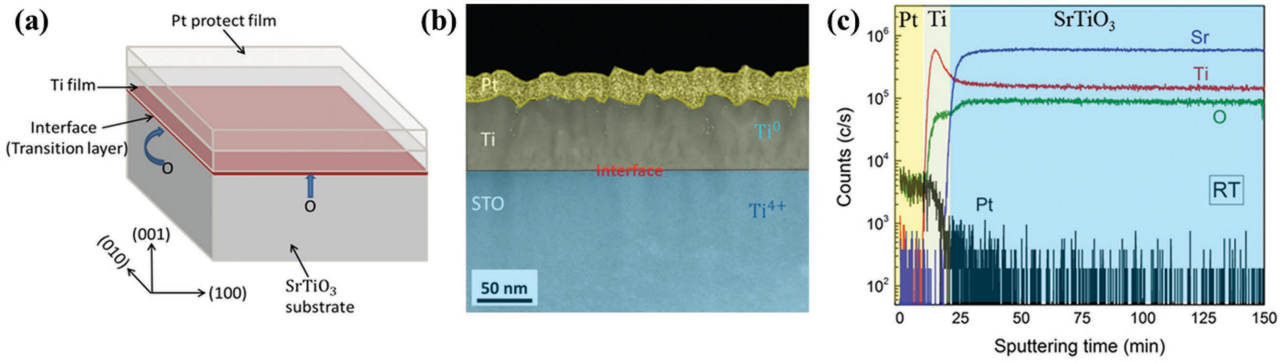

Figure 1. a) Schematic representation of the Pt/Ti/STO heterostructure. Thin films of 65 nm Ti and 50 nm Pt (protecting layer) were deposited on a (001) STO substrate using magnetron sputtering. b) Cross-section STEM image of the Ti/STO interface. c) SIMS depth profiles of the Pt/Ti/STO samples deposited at room temperature.

2. Experimental Results

2.1. Sample Growth and TEM Characterizations

Figure 1a is the schematic representation of the Pt/Ti/STO structure. The purpose of the top Pt layer is to protect the sample surfaces from mechanical damages during processing. The samples were prepared using direct current magnetron sputtering, and the thicknesses of the Pt and the Ti layers are 50 and 65 nm, respectively. Focused ion beam (FIB) and Ar ion beam milling were used to prepare the TEM lamella. The cross-section of the Pt/Ti/STO structure was characterized using an FEI aberration-corrected Titan Cubed transmission electron microscope operated at 300 kV. The evolution of oxidation state across the interface was obtained from the line scans of the EELS. More details on the fabrication and characterizations of the Pt/Ti/STO samples are described in the Experimental Section. The cross-section STEM image of the Pt/Ti/STO structure is shown in Figure 1b. The top Pt layer appears to be continuous, providing full coverage and surface protection.

To investigate the chemical evolution at the Ti/STO interface, SIMS measurements were performed under the ultrahigh vacuum condition. The raw depth profiling data, displayed in Figure 1c, show the variation of O, Pt, Ti, and Sr signals as a function of the sputtering time for the sample deposited at room temperature. The most striking observation is the variation of the oxygen intensity at the Ti/STO interface as a result of oxygen diffusion. Interestingly, a clear oxygen signal was observed in the Ti layer, which is accompanied by a notable drop of the oxygen level in the STO substrate near the interface. Furthermore, a notable increase of the Ti signal was observed in STO in the same interface region, which could be associated with the high-concentration oxygen vacancies due to the matrix effect.[25,26]

High-resolution HAADF-STEM images of the metal/oxide interface prepared at room temperature are shown in **Figure 2**. Surprisingly, in the overview [100] HAADF-STEM image (Figure 2a) collected at the Ti/STO interface, we observed an ultrathin well-defined crystalline layer of TiO_x, which is formed as a result of interfacial oxygen diffusion. In such STEM observations, Sr atoms exhibit much brighter contrast than Ti atoms due to their much higher Z number. The lattice structure of this interfacial layer, as shown in Figure 2b, appeared to be similar to the STO substrate. However, different from the STO substrate, no Sr atom was observed in this ultrathin layer. Figure 2c shows the HAADF signal profile along with the image. The TiO_2 termination layer on the STO single crystal substrate surface was clearly observed, and the crystalline structure above the TiO_2 layer seems to exist mostly within one atomic layer. Most likely, Ti atoms react with the oxygen from the STO substrate, and the crystalline structure of the formed TiO_x monolayer strictly follows that of the STO substrate underneath. Discontinuous Ti-containing crystalline structures also appear to exist in a couple of atomic layers above this TiO_x layer, but the contrast in the HAADF images is much weaker.

As a reference, a high-resolution HAADF-STEM image and a HAADF signal profile were also collected at a Pt/STO interface sample prepared under identical experimental conditions. As shown in the Figure 2d, no extra oxidized layer was observed above the TiO_2-terminated STO substrate surface. Apparently, the structural differences between the Ti/STO and the Pt/STO interfaces are a result of the metal property: the noble metal Pt does not react with the oxygen ions from the STO substrate, while Ti is much more active and react with the oxygen ions diffused from the STO substrates. It is important to note that this atomic-scale oxidation reaction at the Ti/STO interface occurs even at room temperature, which thermodynamically requires no external activation.

2.2. EELS Characterizations of the Ti/STO Interface

To shed light on the evolution of Ti oxidation states at the Ti/STO interface, we used EELS to investigate the samples. EELS is a powerful technique to study the element distribution and valence states at the atomic level.[27,28] In the EELS experiments, we analyzed the energy of the transmitted electron beam and performed the core level spectroscopy at the atom level. This technique allowed us to directly probe the internal structures at the Ti/STO interface, unlike surface-sensitive methods. As shown in Figure S1 (Supporting Information), EELS spectra were collected from three locations: inside the Ti layer (far from the interface), at the Ti/STO interface, and inside the STO substrate (far from the interface). As expected, the EELS spectra of the Ti layer and the STO substrate are in line with the reports

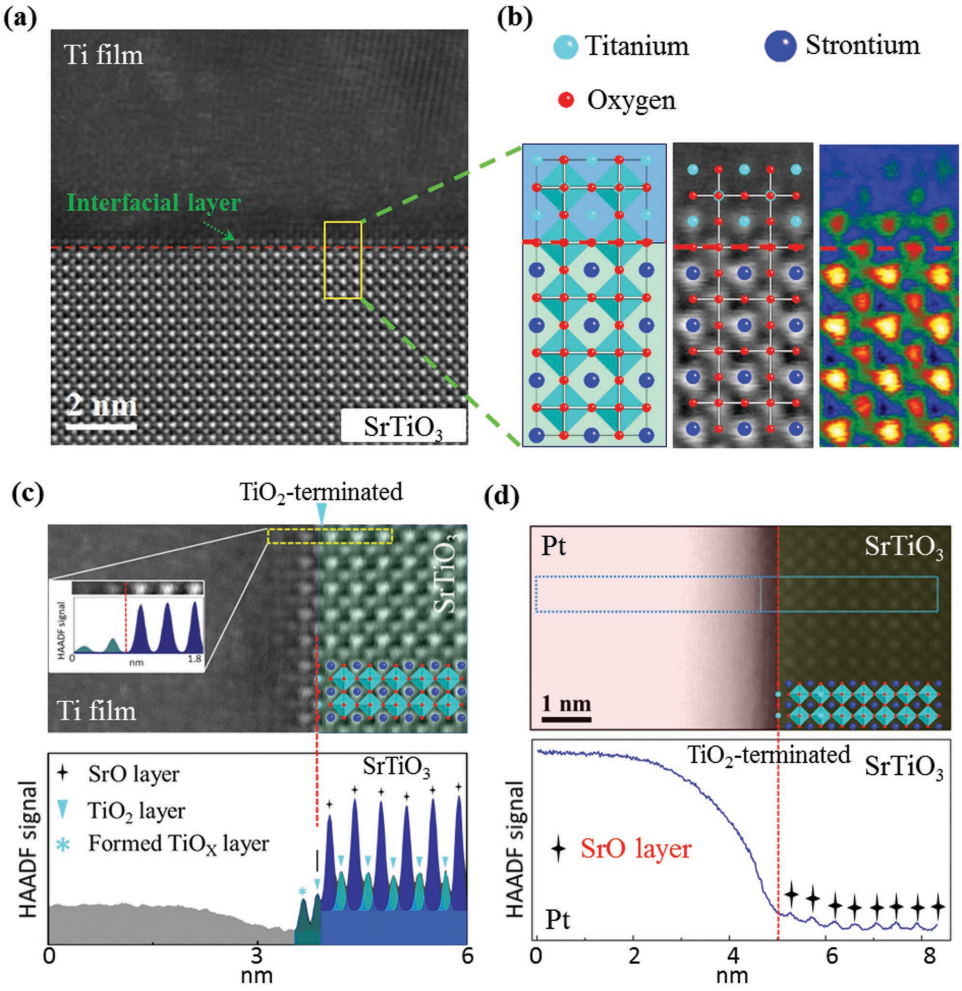

Figure 2. a) HAADF-STEM image of the Ti/STO interface prepared by sputtering Ti at room temperature. b) The images, from left to right, are lattice structure, high resolution HADDF-STEM image (in Grayscale) overlaid with supposed structure and high resolution HADDF-STEM image (in Temperature scale) for the area marked with a yellow rectangle in (a), respectively. O: red. Sr: blue. Ti: cyan. c) High-resolution HAADF-STEM image (upper) for the cross-section of Ti/STO interface, at a smaller scale than (a). And the HAADF signal profile, obtained from the whole above image, was shown at the bottom. HAADF signal profile for the yellow dashed line squared area was inserted. d) High resolution HAADF-STEM image (upper) for the cross-section of Pt/STO interface, deposited at room temperature, and the HAADF signal profile, obtained from the blue rectangle area, was shown at the bottom. Red dashed lines in this figure and others mark the TiO_2 termination layer of the STO substrate.

on Ti^0 and Ti^{4+} oxidation states, respectively. As shown in Figure S1a (Supporting Information), four peaks, i.e., t_{2g} (L_3) at 459.64 eV, e_g (L_3) at 462.92 eV, t_{2g} (L_2) at 465.18 eV, and e_g (L_2) at 467.26 eV were observed in the Ti^{4+} spectra. In contrast, there are only peaks of e_g (L_3) at 458.91 eV and e_g (L_2) at 464.61 eV observed in the Ti^0 spectra. More importantly, as shown in Figure S1b (Supporting Information), the Ti-$L_{2,3}$ edge spectrum collected from the interface appears to be much more complex, and it cannot be taken as a simple superposition of the spectra from the Ti layer (Ti^0) and the STO substrate (Ti^{4+}).

In order to investigate in detail the evolution of Ti oxidation states across the Ti/STO interface, EELS line scans were collected at the atomic level. **Figure 3** shows the data taken on the sample deposited at room temperature. Specifically, the titanium $L_{2,3}$ (Ti-$L_{2,3}$) and oxygen K (O-K) edges can be simultaneously recorded, with an energy resolution of ≈0.1 eV and a spatial resolution of ≈0.4 nm. We performed a line scan from the Ti layer to the STO substrate, crossing the Ti/STO interface. Figure 3a presents the scan direction and position, which overlays with the high-resolution HAADF-STEM image of the Ti/STO interface. The region of EELS line scans has a length of 9.6 nm. The background-subtracted EELS spectra for both Ti-$L_{2,3}$ and O-K edges are shown in Figure 3b, and the valence evolutions of Ti and O appear to occur gradually. The spectra, at the interface and the points where Ti oxidation states change, are highlighted. As references, as-received STO substrate and commercial Ti_2O_3 powder were also measured, and their EELS data are shown in Figure S2 (Supporting Information). In the spectra of Ti-$L_{2,3}$ edge shown in Figure 3b, peak broadening and less pronounced peak splitting were clearly observed at the Ti/STO interface, which could be attributed to the presence of Ti^{3+} valence.[29] Here, it should be noted that we cannot exclude the existence of Ti^{2+} between the Ti^{3+} and Ti^0 layer. As shown in Figure S3 (Supporting Information), the EELS spectra for

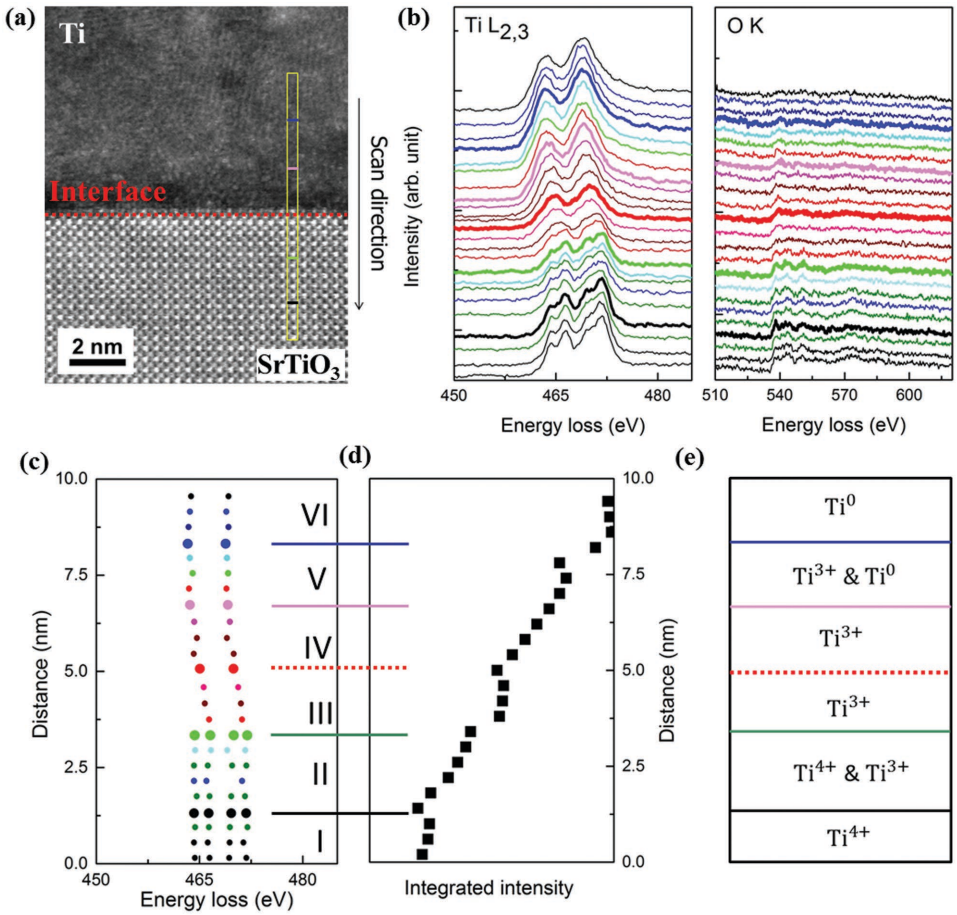

Figure 3. a) High resolution HAADF-STEM image of the Ti/STO interface prepared at room temperature. (b) EELS spectra of Ti-$L_{2,3}$ and O-K edges obtained from line scans across the interface shown in (a). The spacing along the line scan between consecutive EELS spectra is 4 Å. The spectra at the interface and the evolution points with different oxidation states are highlighted by thicker lines. For the spectra of Ti-L_2 and Ti-L_3, peak broadening and less pronounced peak splitting at the interface were clearly observed, indicating the valence evolution of Ti (from Ti^{4+} to Ti^{3+}, and then to Ti^0). c) Peak positions of Ti-$L_{2,3}$ edges. d) Evolution of the integrated intensity of O EELS edges. The gradual fading intensity indicates the oxygen diffusion from the STO substrate to the Ti layer. e) Schematic presentation for the evolution of Ti oxidation states across the Ti/STO interface.

Ti^{2+} and Ti^{3+} are quite similar, especially at the Ti-$L_{2,3}$ edge (two peaks).[30] Moreover, the intensity of the O-K edge is weak and noisy, which cannot be used to distinguish Ti^{2+} from Ti^{3+}.

Figure 3c shows the peak positions of Ti-$L_{2,3}$ edge along the line scan direction. Clearly, the Ti-$L_{2,3}$ oxidation states change from Ti^{4+} in the STO substrate to Ti^{3+} at the interface, then to Ti^0 in the Ti metal layer. The interfacial region with the dominant Ti^{3+} oxidation state spans ≈3.2 nm. Figure 3d shows the integrated intensity of O-K edge as a function of the distance from the interface. The decrease of oxygen intensity from the STO substrate to the Ti layer illustrates the chemical evolution of the content as a result of the oxygen diffusion from the oxygen-rich STO to the oxygen-less Ti. Comparison of Figure 3c,d indicates the strong correlation of the evolution of Ti oxidation states and the oxygen diffusion. Overall, in this Ti/STO sample prepared at room temperature, the oxidation of the Ti layer and the reduction of the STO substrate occur within an interfacial region with a thickness of 6.8 nm.

Based on the EELS spectra of Ti-$L_{2,3}$ and O-K edges, we distinguished the nanoscale evolution of oxidation states at the Ti/STO interface as six regions, as shown in Figure 3e. The region I is featured by four clear and sharp peaks at the Ti-$L_{2,3}$ edge, indicating the characteristic Ti^{4+} ions in STO. The integrated intensity of oxygen remains constant in this region (Figure 3d). In the region II, the integrated oxygen intensity starts to decrease from the STO substrate to the Ti layer, as a result of the oxygen diffusion. Concurrently, Ti^{4+} partially changed into Ti^{3+}, in order to maintain the charge neutrality in the region. As shown in Figure 3b,c, the four peaks at the Ti-$L_{2,3}$ edge became broader, with peak separations less pronounced, and even part of the t_{2g} peaks at the Ti-$L_{2,3}$ edge could not be unambiguously identified, demonstrating the existence of Ti^{3+}.[29] In the region III, the integrated intensity of oxygen-related EELS peaks keeps decreasing, and the EEL spectra of Ti-$L_{2,3}$ edge shows the characteristic two-peak feature of Ti^{3+} shown in Figure 3b. In the region IV, oxygen signal was detected in the Ti layer, indicating the oxygen diffusion into the metal Ti layer. In this region, the EEL spectra of Ti-$L_{2,3}$ edge still shows the feature of Ti^{3+} (Figure 3b), indicating the formation of a TiO_x (Ti_2O_3-like) interfacial layer. In the region V, the two peaks of Ti-$L_{2,3}$ edge slightly shift to lower energies, indicating the emergence of the Ti^0 component. Finally, in the region VI,

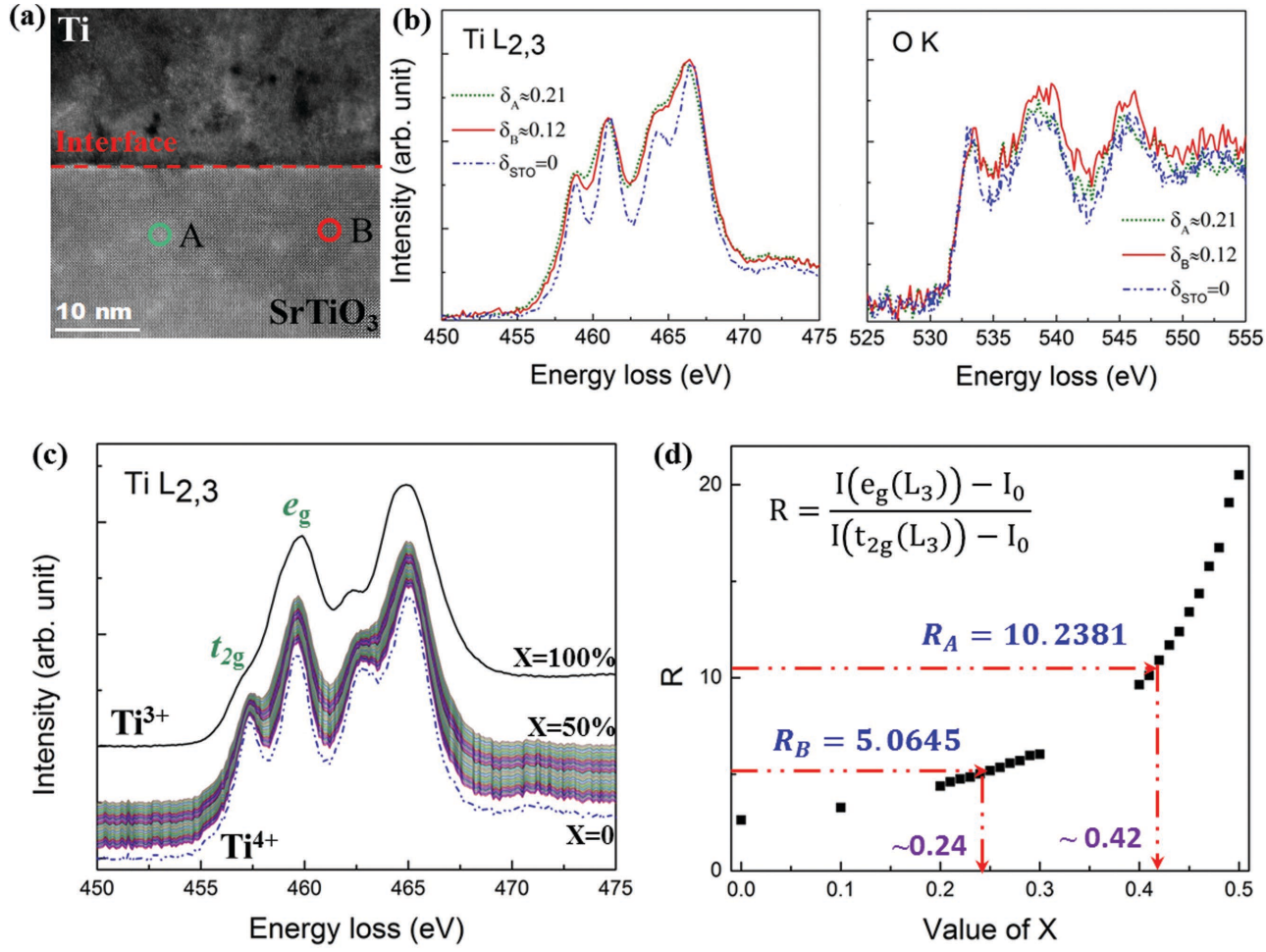

Figure 4. a) LAADF-STEM image of the room-temperature Ti/STO interface sample. Scale bar: 5 nm. Two marked areas were chosen for EELS measurements. b) EELS spectra of Ti-$L_{2,3}$ and O-K edges obtained from those two domains shown in (a), compared with the stoichiometric STO. c) EELS fitting according to $I = X \times < Ti^{3+} > + Y \times < Ti^{4+} >$, with the constraint that $X + Y = 1$. The EELS spectra for Ti^{3+} and Ti^{4+} were taken from the commercial Ti_2O_3 powder and the stoichiometric STO substrate, respectively. d) Parameter $R = \frac{I(e_g(L_3)) - I_0}{I(t_{2g}(L_3)) - I_0}$ plotted as a function of X. We set the intensity for the valley point between $e_g(L_3)$ and t_{2g} (L_3) as I_0. The values of R and X for the areas A and B are highlighted.

the integrated intensity of oxygen decreased to the minimum, and the EELS data at the Ti-$L_{2,3}$ edge indicate the pure Ti^0 in the Ti metal layer. Moreover, theoretical fitting was performed, and as shown in Figure S4 (Supporting Information), the result is consistent with the profiles of experimental line scans. Interestingly, each region with different Ti oxidation states has a thickness of ≈1.6 nm, and the overall chemical and valence evolutions occur within a thickness of ≈6.8 nm (regions II, III, IV, and V) at the interface, and the TiO_x (Ti_2O_3-like) alloy layer in regions IV and V has a thickness of 3.2 nm.

2.3. Observation of Oxygen-Deficient Domains

It is well recognized that oxygen vacancies are ubiquitous in oxides, and their characteristics are important to understand the physical properties of oxides and to harness their functionalities. There are few reports on how oxygen vacancies are distributed at metal/oxide interfaces because interfaces are buried underneath the top layers and difficult to directly probe. Atomic-scale study of oxygen vacancy profiles in STO was carried out in 2004 using LAADF imaging and EELS.[27] The LAADF images record dechanneling from the strain field surrounding the oxygen vacancies, while the HAADF images are sensitive mostly to atomic number. In order to image the oxygen vacancies, we decreased the ADF inner angle from 70 to 25 mrad to switch from the HAADF imaging mode to the LAADF mode.

Figure 4 shows the LAADF image and the EELS analysis of oxygen-deficient domains near the Ti/STO interface prepared at room temperature. Some small domains with sizes of a few nm and bright contrast to the surrounding areas were observed in the STO substrate (Figure 4a). The oxygen deficiency caused some tiny structural changes in the STO lattice, and the white contrast in the LAADF images evidences the strain field surrounding the oxygen-vacancy-containing domains. In fact, the brightness of the oxygen-deficient domains is directly correlated with the density of oxygen vacancies.[27] To illustrate the

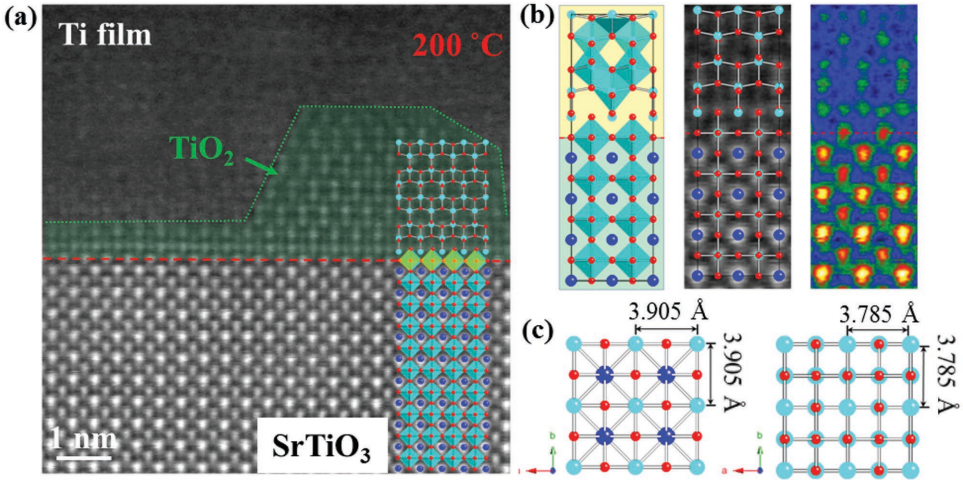

Figure 5. a) High resolution HAADF-STEM image of the Ti/STO interface prepared by depositing Ti at 200 °C. b) From left to right: lattice structure, high-resolution HAADF-STEM image (in the gray scale) with supposed structure and high-resolution HAADF-STEM image (in the "temperature" scale). c) *c*-plane views of STO (left) and anatase-structured TiO_2 (right). Red: O; Blue: Sr; Cyan: Ti.

effectiveness of this approach, two areas (marked with A and B with different contrast in the LAADF imaging) were selected for EELS analysis. Figure 4b shows the EEL spectra of Ti-$L_{2,3}$ and O-K edges from the areas A, B and the stoichiometric STO substrate. These data indicate that the Ti valence shifts from 4^+-like in STO to 3^+-like in oxygen-deficient domains, which is expected since oxygen vacancies are electron donors.

In addition, the O-K edge fine structure is sensitive to the O-O ordering and damps out as the vacancy concentration increases. According to the EELS fittings in Figure 4c, we could obtain the value of δ in $SrTiO_{3-\delta}$ with a precision of 1% for the oxygen-deficient $SrTiO_{3-\delta}$ areas. The reference spectra for Ti^{4+} and Ti^{3+}, used in the fittings in Figure 4c, were taken from a bare STO substrate and commercial Ti_2O_3 powders, respectively. Assuming that the actual EELS spectra at the Ti-$L_{2,3}$ edge is the superposition of Ti^{4+} and Ti^{3+} with different weights, fitting the data to $I = X \times < Ti^{3+} > + Y \times < Ti^{4+} >$, with the constraint of $X + Y = 1$ can be used to reveal the fractional contributions of Ti^{4+} and Ti^{3+}.[31] In order to conveniently link the experimental data with the fitting result, we defined a parameter $R = \frac{I(e_g(L_3)) - I_0}{I(t_{2g}(L_3)) - I_0}$ with I_0 being the intensity of the valley point between $e_g(L_3)$ and $t_{2g}(L_3)$ peaks for each Ti-$L_{2,3}$ spectrum. Then, we obtained the value of R for each spectrum of Ti-$L_{2,3}$ edge., which has a one-to-one correspondence with the value of X (Figure 4d). As examples, R (X) values calculated from the experimental spectra, taken from the oxygen-deficient areas A and B, are 10.2381 (0.42) and 5.0645 (0.24), respectively. Since one oxygen vacancy in $SrTiO_{3-\delta}$ will result in two Ti^{3+} ions, the value of δ should be half of X. Thus, the values of δ for area A and B are ≈0.21 and ≈0.12, respectively, which falls in the range of δ reported for similar oxygen-deficient $SrTiO_{3-\delta}$ films.[27]

2.4. Properties of Ti/STO Interfaces Prepared at Higher Temperatures

Temperature of the STO substrate during the Ti layer growth is clearly an important parameter because more substantial oxygen diffusion is expected at the Ti/STO interface at higher temperatures. In order to investigate the temperature dependence, we prepared another Ti/STO interface sample by depositing the Ti metal layer at 200 °C. As shown in **Figure 5**, the HAADF-STEM image of the 200 °C sample significantly differs from the room temperature one. An inhomogeneous interfacial layer with nm-scale crystalline domains was observed in the Ti side near the interface. Interestingly, the high-resolution HAADF image and its fast Fourier transform (Figure S5, Supporting Information) indicate that the lattice of this interfacial layer is consistent with that of anatase TiO_2. In fact, the in-plane lattice parameters of TiO_2 match well with those of STO, as shown in Figure 5c. The anatase TiO_2 has a tetragonal structure ($a = b = 3.785$ Å; $c = 9.514$ Å), while STO has a cubic structure ($a = 3.905$ Å). According to Figure 5a and Figure S5 (Supporting Information), the "epitaxial" relationship is [100]TiO_2//[100] STO with in-plane mismatch of ≈3.1%. This small lattice mismatch resulted in the formation of nanoscale TiO_2 domains on the STO when the sample was prepared at 200 °C. In fact, the higher oxygen content in this interfacial layer, compared to the TiO_x layer observed in the room temperature sample, is in line with the more substantial oxygen diffusion from the STO substrate to the Ti metal layer at the higher growth temperature.

As expected, larger oxygen-vacancy domains were observed at higher temperature (200 and 600 °C) samples, which are shown in Figure S6 (Supporting Information). Much larger and brighter areas are observed in the LAADF images obtained on these higher temperature samples, which is consistent with the more oxygen diffused from STO to Ti expected at higher temperatures. Moreover, for the sample prepared at 600 °C, the EELS data shown in Figure S6 (Supporting Information) indicate that the whole Ti layer was oxidized by the oxygen diffused from the STO substrate.

3. First-Principles Calculations of the Ti/STO Interface

As one of the most important findings in this work, an ultrathin (one unit cell) Ti_2O_3-like layer was discovered at the Ti/STO

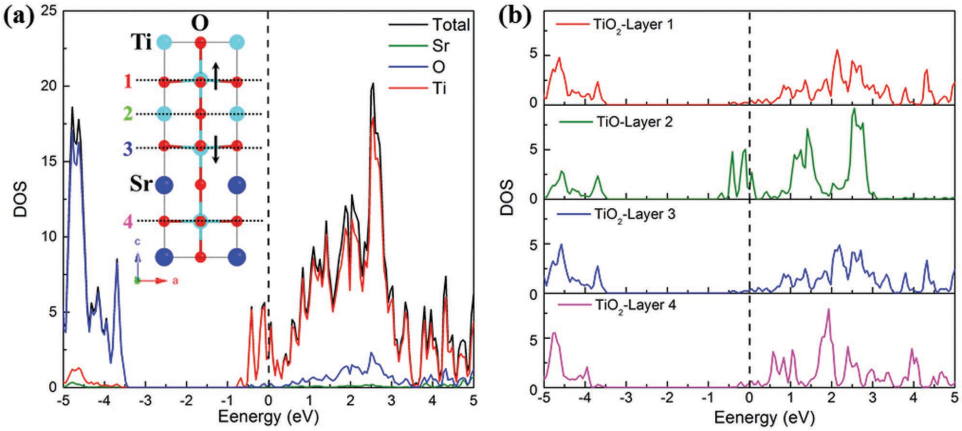

Figure 6. a) Total DOS and atomic pDOS of the Ti_2O_3/STO interface calculated using the HSE method. The crystal structure of the interface is shown as the inset. b) Layer-resolved pDOS of TiO_2 and TiO planes shown in the inset of (a). The Fermi level is positioned at zero, around which the states mostly come from the Ti ions in Layer 2.

interface fabricated at room temperature. In a general perspective, our experiments provide a viable approach toward the synthesis of atomic thin oxide layers. It could be expected that the property of this TiO_x layer at the Ti/STO interface is different from those of both Ti and STO. However, it is difficult to probe the transport properties of this atomic thin layer because the top metallic Ti layer is highly conductive. Instead, we turned to calculations using density functional theory to predict the possible physical properties of this interfacial layer containing Ti^{3+} ions.

In our calculations, the model Ti_2O_3/STO heterostructure is consisted of two SrO layers, three TiO_2 layers, and one TiO layer, and the relaxed lattice structure is shown as inset in **Figure 6**a. Cubic-structured perovskite Ti_2O_3 ($a = b = c = 3.90$ Å; $\alpha = \beta = \gamma = 90°$) and STO were used in modeling the superlattice. Details of the calculation are shown in the Experimental Section. Based on the generalized gradient approximation (GGA) optimized structure, the hybrid functional calculations based on Heyd–Scuseria–Ernzerhof (HSE) exchange were performed to give a more accurate description of the band structure of this interface. The density of states (DOS) and atomic projected DOS (pDOS) of the interface are shown in Figure 6a. Layer-resolved pDOS results, shown in Figure 6b, indicate that the electronic states around the Fermi energy mainly comes from the contribution of Ti 3*d* orbitals, especially from the sandwiched TiO layer, where a 2D electron gas could be generated. Interestingly, the pseudogap tendency is observed, implying a probable localization of carriers.

As a comparison to the Ti^{3+}-contained interface, we also calculated the band structure of bulk Ti_2O_3 using the same HSE method. Bulk Ti_2O_3 usually features a corundum (trigonal) lattice ($R\bar{3}c$ space group, #167; $a = b = 5.15$ Å, $c = 13.61$ Å; $\alpha = \beta = 90°$, $\gamma = 120°$), and it is a narrow band gap (≈0.1 eV) semiconductor.[32] The total DOS of the cubic Ti_2O_3/STO interface and bulk Ti_2O_3 is shown in Figure S7 (Supporting Information). As expected, a band gap of 0.09 eV was obtained for bulk corundum Ti_2O_3, which is in contrast to the metallic cubic-structured Ti_2O_3/STO interface. It would be interesting to etch off the top Ti layers from the Ti/STO interface samples and to directly probing the physical properties of the Ti_2O_3/STO interface, which is however out of the scope of this work.

4. Conclusion

In summary, we characterized the chemical and valence evolution at the Ti/STO interface using complementary microscopic techniques. Interestingly, an atomic-thin Ti_2O_3-like interfacial layer was observed at the Ti/STO interface in the sample deposited at room temperature. Furthermore, oxygen vacancies were generated in the STO substrates in all samples, and the density and size of oxygen-deficient domains increases with the Ti deposition temperature. When the Ti deposition temperature increased to 200 °C, we observed an ultrathin continuous TiO_2 interfacial layer between the STO substrate and nanoscale island-like domains of crystalline anatase TiO_2. Clearly, such metal/oxide interfaces are far from atomically sharp as people usually perceive, and the interfacial phases with varied Ti oxidation states must be carefully considered. In addition, our calculation results suggested that the ultrathin Ti_2O_3 (Ti^{3+})/STO interface possesses metallic transport properties and may serve as a 2D electron gas system in future studies. Overall, our work demonstrated the intricate nanoscale chemical and valence evolution at the Ti/STO interface as a prototypical metal/oxide system, providing insights on the operation of interface-based devices.

5. Experimental Section

Sample Preparation: The Ti layer with thickness of ≈65 nm was deposited on a single crystal STO (001) substrate by direct current magnetron sputtering. Ti target with purity 99.999% was used in the sputtering process. Note that the TiO_2-termination of our substrates were obtained by chemical etching using HCL-HNO_3 as acidic solution,[33] which was found to produce less defects on the STO surface compared with the conventional buffered hydrofluoric acid etch method.[34,35] The base pressure of the chamber before deposition was better than 2.0×10^{-7} Torr. During the deposition, the Ar pressure was kept at 5.0 mTorr with Argon flow (20 SCCM). The sputtering power was fixed at 150 W. The substrate temperatures were maintained at room temperature, 200, and 600 °C, respectively. Prior to the deposition, Ti target was presputtered for 20 min, inside of the chamber, to remove the oxidation layer on the surface of Ti target and the oxygen in the chamber. After the deposition, ≈50 nm Pt thin films were deposited on the samples without breaking the vacuum to prevent the oxidation.

Transmission Electron Microscopy: Focused ion beam (FEI Helios 400S) had been used to prepare the cross-section samples for S/TEM analysis. S/TEM lamella of ≈100 nm thick had been transferred to a half moon FIB grid by the in situ lift out method, followed by a low kV cleaning of Ar ion in a Fischone Nano Mill 1040. The damaged layer during FIB preparation had been removed and the final thickness of the sample was ≈20 nm. Part of the Pt layer was removed during the S/TEM specimen preparation. To avoid oxidation, these samples were transferred to the TEM, immediately. Then, the cross-section of the Pt/Ti/STO structure was characterized by Mono-Probe Cs scanning transmission electron microscope (Titan, FEI). Electron diffraction patterns were obtained with a TitanST electron microscope operated at 300 kV. HAADF-STEM images were obtained with aberration-corrected Mono-Probe Cs scanning transmission electron microscope (Titan, FEI) operated at 300 kV using the convergence semiangle of 21 mrad. The inner collection semiangle of the HAADF was 70 mrad.

SIMS: SIMS depth profiling experiments were performed using a dynamic SIMS instrument from Hiden Analytical company (Warrington-UK) operated under ultrahigh vacuum conditions (typically 10^{-9} Torr). The dynamic SIMS was equipped with an argon gas source. Throughout the sputtering process, the selected positive ions were sequentially collected using a MAXIM spectrometer equipped with a quadrupole analyzer. After passing through a triple filter system, ions were measured using a pulse counting detector having a 4 keV post acceleration potential to increase the detection efficiency at high masses.

First-Principles Calculation: The calculations were performed based on the projector augmented wave approach as implemented in the Vienna ab initio simulation package.[36–38] The electronic correlation was treated in terms of the GGA with Perdew–Burke–Ernzerhof functional modified for solids parametrization.[39] The structural optimization and electronic self-consistent interactions were performed using a plane-wave cut-off 500 eV and a Γ-centered Monkhorst–Pack k-point mesh of $7 \times 7 \times 5$. Both the out-of-plane lattice vector c and the internal atomic positions were fully optimized until the Hellman–Feynman forces converged to within 10 meV $Å^{-1}$, while the other two in-plane lattice constants were fixed to the substrate. Based on the GGA optimized structure, the hybrid functional calculations based on HSE exchange were also performed to pursuit a better description of band structure.[40] Due to its extreme demand of CPU-time, the k-point mesh was reduced to $5 \times 5 \times 2$ in the HSE calculation.

Supporting Information

Supporting Information is available from the Wiley Online Library or from the author.

Acknowledgements

This work was supported by the King Abdullah University of Science and Technology (KAUST). M.A. and S.D. were supported by the National Natural Science Foundation (Grant No. 11274060). The experiments were performed in the Nanofabrication & Thin Film core lab, and the Imaging & Characterization Core Lab in KAUST.

Received: March 10, 2016
Revised: May 17, 2016
Published online:

[1] S. Nakamura, T. Mukai, M. Senoh, *Jpn. J. Appl. Phys.* **1995**, *34*, L687.
[2] S. Nakamura, M. Senoh, S. Naghama, N. Iwasa, T. Yamada, T. Matsushita, H. Kiyoku, *Jpn. J. Appl. Phys.* **1996**, *35*, 74.
[3] S. Nakamura, M. Senoh, S. Nagahama, N. Iwasa, T. Yamada, T. Matsushita, H. Kiyoku, Y. Sugimoto, T. Kozaki, H. Umemto, M. Sano, K. Chocho, *Jpn. J. Appl. Phys.* **1997**, *36*, L1568.
[4] J. S. Foresi, T. D. Moustakas, *Appl. Phys. Lett.* **1993**, *62*, 2859.
[5] J. Burm, K. Chu, W. A. Davis, W. J. Schaff, T. J. Eustis, L. F. Eastman, *Appl. Phys. Lett.* **1997**, *70*, 464.
[6] B. P. Luther, S. E. Mohney, T. N. Jackson, M. A. Khan, Q. Chen, J. W. Yang, *Appl. Phys. Lett.* **1997**, *70*, 57.
[7] Z. F. Fan, S. N. Mohammad, W. Kim, O. Aktas, A. E. Botchkarev, H. Morkoc, *Appl. Phys. Lett.* **1996**, *68*, 1672.
[8] B. P. Luther, J. M. DeLucca, S. E. Mohney, R. F. Karlicek Jr., *Appl. Phys. Lett.* **1997**, *71*, 3859.
[9] J. Robertson, C. W. Chen, *Appl. Phys. Lett.* **1999**, *74*, 1168.
[10] H. Stocker, M. Zschornak, J. Seibt, F. Hanzig, S. Wintz, B. Abendroth, J. Kortus, D. C. Meyer, *Appl. Phys. A* **2010**, *100*, 437.
[11] M. Mrovec, J. M. Albina, B. Meyer, C. Elsasser, *Phys. Rev. B* **2009**, *79*, 245121.
[12] J. F. Schooley, W. R. Hosier, E. Ambler, J. H. Becker, *Phys. Rev. Lett.* **1965**, *14*, 305.
[13] D. Kan, T. Terashima, R. Kanda, A. Masuno, K. Tanaka, S. Chu, H. Kan, A. Ishizumi, Y. Kanemitsu, Y. Shimakawa, M. Takano, *Nat. Mater.* **2005**, *4*, 816.
[14] D. Kan, R. Kanda, Y. Kanemitsu, Y. Shimakawa, M. Takano, T. Terashima, A. Ishizumi, *Appl. Phys. Lett.* **2006**, *88*, 191916.
[15] D. Kan, O. Sakata, S. Kimura, M. Takano, Y. Shimakawa, *Jpn. J. Appl. Phys.* **2007**, *46*, L471.
[16] Y. Tokura, Y. Taguchi, Y. Okada, Y. Fujishima, T. Arima, K. Kumagai, Y. Iye, *Phys. Rev. Lett.* **1993**, *70*, 2126.
[17] D. K. Lee, I. S. Cho, D. K. Yim, J. H. Noh, K. S. Hong, D. W. Kim, *J. Ceram. Soc. Jpn.* **2010**, *118*, 876.
[18] H. Y. Peng, L. Pu, J. C. Wu, D. Cha, J. H. Hong, W. N. Lin, Y. Y. Li, J. F. Ding, A. David, K. Li, T. Wu, *APL Mater.* **2013**, *1*, 052106.
[19] K. Zhao, K. J. Jin, Y. H. Huang, S. Q. Zhao, H. B. Lu, M. He, Z. H. Chen, Y. L. Zhou, G. Z. Yang, *Appl. Phys. Lett.* **2006**, *89*, 173507.
[20] Y. H. Huang, K. Zhao, H. B. Lu, M. He, K. J. Jin, Z. H. Chen, Y. L. Zhou, G. Z. Yang, *Eur. Phys. J.: Appl. Phys.* **2007**, *38*, 37.
[21] K. X. Jin, Y. Zhang, B. C. Luo, J. Y. Wang, C. L. Chen, T. Wu, *EPL* **2013**, *103*, 57007.
[22] Q. Fu, T. Wagner, *Surf. Sci. Rep.* **2007**, *62*, 431.
[23] A. J. Francis, Y. Cao, P. A. Salvador, *Thin Solid Films* **2006**, *496*, 317.
[24] S. A. Chambers, M. Gu, P. V. Sushko, H. Yang, C. Wang, N. D. Browning, *Adv. Mater.* **2013**, *25*, 4001.
[25] R. G. Wilson, F. A. Stevie, C. W. Magee, *Secondary Ion Mass Spectrometry—A Practical Handbook For Depth Profiling and Bulk Impurity Analysis*, Wiley, New York **1989**.
[26] M. L. Yu, *Nucl. Instrum. Methods Phys. Res., Sect. B* **1986**, *15*, 151.
[27] D. A. Muller, N. Nakagawa, A. Ohtomo, J. L. Grazul, H. Y. Hwang, *Nature* **2004**, *430*, 657.
[28] H. Tan, S. Turner, E. Yücelen, J. Verbeeck, G. Van Tendeloo, *Phys. Rev. Lett.* **2011**, *107*, 107602.
[29] H. W. Jang, D. A. Felker, C. W. Bark, Y. Wang, M. K. Niranjan, C. T. Nelson, Y. Zhang, D. Su, C. M. Folkman, S. H. Baek, S. Lee, K. Janicka, Y. Zhu, X. Q. Pan, D. D. Fong, E. Y. Tsymbal, M. S. Rzchowski, C. B. Eom, *Science* **2011**, *331*, 886.
[30] C. N. Huang, J. S. Bow, Y. Zheng, S. Y. Chen, N. Ho, P. Shen, *Nanoscale Res. Lett.* **2010**, *5*, 972.
[31] A. Ohtomo, D. A. Muller, J. L. Grazul, H. Y. Hwang, *Nature* **2002**, *419*, 378.
[32] H. Nakatsugawa, E. Iguchi, *Phys. Rev. B* **1997**, *56*, 12931.
[33] Y. Z. Chen, N. Pryds, *Thin Solid Films* **2011**, *519*, 6330.
[34] J. Zhang, D. Doutt, T. Merz, J. Chakhalian, M. Kareev, J. Liu, L. J. Brillson, *Appl. Phys. Lett.* **2009**, *94*, 092904.
[35] S. A. Chambers, T. C. Droubay, C. Capan, G. Y. Sun, *Surf. Sci.* **2012**, *606*, 554.
[36] G. Kresse, J. Hafner, *Phys. Rev. B* **1993**, *47*, 558.
[37] G. Kresse, J. Furthmüller, *Phys. Rev. B* **1996**, *54*, 11169.
[38] P. E. Blochl, *Phys. Rev. B* **1994**, *50*, 17953.
[39] J. P. Perdew, A. Ruzsinszky, G. I. Csonka, O. A. Vydrov, G. E. Scuseria, L . A. Constantin, X. Zhou, K. Burke, *Phys. Rev. Lett.* **2008**, *100*, 136406.
[40] J. Heyd, G. E. Scuseria, M. Ernzerhof, *J. Chem. Phys.* **2003**, *118*, 8207.